Stabilising the tetrahedral defect configuration in nematic shells

Martin A. Bates[a]*

[a] *Department of Chemistry, University of York, York YO10 5DD, United Kingdom*

*email: martin.bates@york.ac.uk

Stabilising the tetrahedral defect configuration in nematic shells

Monte Carlo simulations are used to investigate the director configurations and the arrangements of the disclination lines that form in nematic shells surrounding interior spherical and polyhedral particles. For nematic shells formed around an interior spherical particle, a tetrahedral arrangement of the disclination lines is observed but this arrangement is lost if the interior sphere is shifted from the centre. The simulations indicate that a narrower angular distribution is observed for interior tetrahedral particles and, for non-centrosymmetric shells, the distribution is significantly less broadened compared to similar spherical inclusions. Other shape polyhedral particles are shown to give disclination geometries of different symmetries.

Keywords: Monte Carlo; nematic shells; disclination lines; defects

Introduction

Nematic shells are a layer of liquid crystal enclosing a central core [1-8]. In its simplest form, a nematic shell can be prepared as a water-in-oil-in-water double emulsion droplet, in which a spherical water droplet is confined inside a spherical nematic droplet suspended in water [3,9]. However, the inner and/or outer surfaces do not necessarily need to be liquid-liquid interfaces and similar topologies would be formed for (hard) colloidal particles trapped inside nematic droplets, for example. Indeed although early experiments were based on liquid inclusions, nematic shells formed around non-liquid inclusions have recently been prepared experimentally [10]. The interest that nematic shells have attracted in the soft matter community originates in the frustration in the director field imposed by the confinement and alignment at the two surfaces, which inevitably leads to the presence of defects in the nematic region. If the alignment at both the inner and outer surface is planar, then the Poincaré-Hopf constraint [1,11] requires that the total defect charge on each surface must equal +2. While this can be achieved in many ways, the lowest energy state for this to occur for ‘thin’ shells (ones in which

3D escaped defects do not occur) results in four +1/2 disclination lines that repel equally and thus form at the vertices of a tetrahedron (see, for example, [8]); here the charge +1/2 corresponds to a rotation in the director field of 180° on a path encircling the defect. Previous Monte Carlo simulations [4] have shown that the tetrahedral disclination line structure is indeed stable for sphere-in-sphere type geometries and that the disclination geometry can be varied by the applying an aligning field to change the internal ordering of the nematic inside the shell. Since the disclinations are locally disordered and thus high energy regions of these colloidal objects, it has been speculated that they could potentially be chemically attacked and 'ligands' attached in a tetrahedral arrangement which could lead to objects capable of forming self-assembling complex architectures [2]. However, experiments on double emulsion droplets highlight a significant problem, in that if the central spherical droplet is not concentric with the outer surface then the total elastic energy can be minimised by the disclination lines locating in the thinner regions of the shell. Thus for non-concentric spherical inclusions, the tetrahedral geometry is not favoured; this has also been confirmed by previous simulations [7].

Since most experimental studies to date have been concentrated on double emulsion droplets, most theoretical and simulation work has also concentrated on sphere-in-sphere type shells. Non-spherical (ellipsoidal) particles have previously been considered using simulations [6] and more recently experimentally using polystyrene particles [10], albeit here with a radial director field due to homeotropic anchoring at the surfaces. In this paper, given the recent advances in trapping 'hard' non-spherical particles inside droplets to form nematic shells, we use Monte Carlo (MC) simulations of a liquid crystal model to investigate whether using polyhedral colloidal particles, in particular tetrahedral ones, inside nematic droplets can stabilise the tetrahedral

configuration for the disclination lines, for both centrosymmetric and non-centrosymmetric shells. We also extend the simulations to other polyhedral particles with a larger number of vertices to investigate the influence of the particle shape on the possible configurations adopted by the disclinations.

Model

We have used the well-known Lebwohl-Lasher (LL) model for nematics [12,13], which has been used extensively for the study of both bulk [13] and especially confined liquid crystals [4,6-8,14] where large length-scales are required. In this model, simple headless rotors interact with their neighbours on a cubic lattice through the potential $-\varepsilon_{ij}\left(\frac{3}{2}(\boldsymbol{u}_i \cdot \boldsymbol{u}_j)^2 - \frac{1}{2}\right)$ where $\boldsymbol{u}_i$ is a unit vector representing the orientation of rotor *i*, and the energy parameter $\varepsilon_{ij} = \varepsilon$ ($\varepsilon > 0$) for nearest neighbours and zero otherwise. This choice of potential favours the parallel alignment of two neighbouring rotors and thus can lead to an orientationally ordered nematic liquid crystalline phase at low enough temperature; the transition from the isotropic to the nematic phase occurs at $T^*_{NI} = 1.1232$ (see below) [13]. As for previous simulations of nematic shells [4,6-8], ghost particles are used to define the anchoring at the surfaces. These extra sites are fixed in orientation, such that they are perpendicular to the surface and interact with the neighbouring spins inside the nematic shell via the LL potential with the energy parameter $\varepsilon_{ij} = -\varepsilon$. This choice of energy parameter favours perpendicular alignment between a rotor representing the nematic liquid crystal and a neighbouring ghost site, thus forcing planar anchoring at the surface. In principle, the anchoring strength can be varied by varying this parameter. However, varying the strength does not change the generic behaviour of the results and so only results with this particular choice will be presented here.

All simulations were run for a system based on an outer spherical surface of radius 40a, where a is the lattice spacing of the model. Dimensions of the interior inclusions will be given in the relevant sections and all are in terms of the lattice spacing a. For small interior inclusions, 'thick' nematic shell behaviour was observed (see, for example, Ref. [8] and Figure 1(d)); thus 3D escaped defects occured, where the director field becomes parallel to the surface normal within the nematic region. In this paper, only the larger inclusions for which 'thin' shell behaviour is observed (see Figures 1(a) to (c)) will be discussed. It should be pointed out that comparisons of the dimensions at which the cross-over from 'thick' to 'thin' behaviour occurs for the model with those of existing experimental systems is somewhat difficult to make since, even though the model is relatively simple, the typical system sizes in simulations are rather small in comparison. For example, if we assume that each lattice site is an orientationally ordered fluid region of roughly 100 molecules, within which the director is relatively well defined and constant, then the dimension a turns out to be roughly 40Å for typical rod-like mesogens; hence, the diameter of the simulation droplet is of the order of a few hundred nanometers. This is about three orders of magnitude smaller than experimental droplets, where the diameters are typically of the order of a few hundred microns. The actual thickness of the nematic shell is likely to have some bearing on the stability of the different configurations, and especially the transitions between them, and so it is important not to just focus on the relative ratio of inner to outer diameters. Thus, whilst it might be tempting to make comparisons between simulation and experiment for the relative ratio at which 'thick' or 'thin' behaviour should occur, some care needs to be taken here; we might expect (and indeed we observe) 'thin' behaviour in relatively thick shells in simulations partly as the nematic layers are actually thin in absolute terms. However, that said, the interactions between the disclinations in a particular type

of configuration are likely to be very similar. That is, for example, all (homeogenous) 'thin' shells with four +1/2 disclinations should have similar tetrahedral arrangements, whatever their absolute size; however, the ratio at which they become 'thin' will vary depending on the absolute size.

The simulations were started from an isotropic configuration generated by randomising the orientation of each nematic rotor. The temperature (dimensionless, defined as $T^* = k_B T / \varepsilon$) was then slowly reduced from just above T^*_{NI} to $T^* = 1.0$ over 500,000 MC cycles, where one cycle corresponds to, on average, one rotational trial per nematic rotor. The simulations were then extended by a further 250,000 cycles during which the locations of the disclinations and the director configurations were determined. Once the defect lines have formed, their motion is typically very slow and so, in order to ensure that we are probing the possible configurations effectively, the simulations were each run multiple times using different initial random number seeds each time both to generate the starting configurations and in the subsequent MC trials; concentric spherical systems were run 100 times, non-concentric spherical systems 250 times, all tetrahedral systems 1000 times and all other polyhedral systems 400 times. The disclination lines were identified using the algorithm of Callan-Jones *et al.* [15], in which a local ordering matrix is diagonalised to yield both the local director and a metric that can identify the extent of local order or, more usefully here, disorder; for full details of the implementation to similar lattice based systems, see Refs. [4,6]. To identify the locations of the disclinations at the surfaces, we define a surface region as all points within $2a$ of the surface of interest. Then, all points within that region with a metric below the threshold for identifying disorder were clustered and the centres of these clusters were used to define where the disclinations touch the surface; we use $c_l < 0.30$ (see [4,6] for definition) as the threshold value, although the results are not

sensitive to this. In order to quantify the arrangement of the disclination lines, an angular probability distribution is defined, where the angle of interest is the central angle formed between a pair of defects and the centre of the nematic droplet. For each system type (that is, all simulations for a fixed inclusion shape, size, shift), this distribution is averaged over all discrete pairs of angles, every 1000th cycle and over all repeat simulations. For a perfect tetrahedral arrangement, each pair of defects should have a central angle of 109.47°, independent of the actual orientation of the tetrahedron, and thus this pairwise angular probability distribution can be used to monitor the mutual arrangement of the disclination lines and to what extent disclinations form a tetrahedral geometry or deviate from it.

Results and discussion

Central and shifted spherical inclusions

Nematic shells based on centrosymmetric spherical inclusions have previously been studied [4]. However, to aid comparison with non-centrosymmetric spheres and tetrahedral inclusions, we have run a number of different sized inclusions to determine the angular probability distributions. As shown in Figures 1(a) and (b), thin shell behaviour is observed for large enough inclusions, in that four +1/2 disclination lines are observed and the director field is essentially perpendicular to the surface normal throughout the volume. We note that two different types of director configurations are observed with roughly equal frequency. In Figure 1(a) the director is parallel to the shortest path between linked pairs of defects, whereas in 1(b) it is perpendicular; these are the equivalents of the ‘baseball’ and ‘cricket ball’ seam models of Vitelli and Nelson [16]. On shifting the spherical inclusion away from the centre, it is clear that the disclination lines are also shifted, as shown in Figure 1(c), and so the locations where

these touch the outer surface no longer form the vertices of a tetrahedron [3,7]. This deviation from tetrahedral geometry can be quantified through the angular probability distribution, as shown in Figure 2. In Figure 2(a), the distribution is shown for centrosymmetric spheres of radius 15*a* and 25*a*. Clearly the distributions are peaked around the tetrahedral angle and the size of the inclusion has little effect on the positions of the defects at the outer surface; the larger sphere (or thinner shell) has a slightly narrower distribution. It is also clear that the geometry at the interior surface (shown only for 15*a* for clarity) is essentially equivalent to that for the exterior surface, in the case of centrosymmetric spheres. We note here that the distribution becomes narrower for lower temperatures and somewhat broader for higher temperatures. Figures 2(b)-(d) show how the angular probability distribution varies on slowing shifting the inclusion away from the centre, at fixed distances. For small deviations ($d = 5a$), the distribution starts to broaden with a shoulder appearing at larger angles and, for larger deviations ($d = 10a$ and $15a$) and thus more extreme non-centrosymmetric inclusions, the distribution can be resolved into multiple separate peaks. As shown in Figure 1(c), there are essentially two types of disclination line for non-centrosymmetric spheres; a pair of shorter ones which are mutually close together (low angle) and a pair of longer ones mutually further apart (high angle). Thus we should expect three peaks to be observed, the third peak at an intermediate angle between a short and a long disclination. The intensities of these are expected in the ratio 1:1:4, respectively. The distribution can be fit using a sum of Gaussian functions of the form

$$f(\theta) = \sum_{i=1}^{3} \frac{A\, I_i}{\sigma_i} e^{\frac{-(\theta-\theta_i)^2}{2\sigma_i^2}}$$

where A is a normalisation factor, θ_i and σ_i are the position and standard deviation of the ith peak and I_i is the relative expected intensity as noted above. θ_i and σ_i can then be used to compare distributions as a function of deviation or shape.

It is interesting to note that the total (elastic) energy of the system hardly changes when shifting the inclusion towards the edge of the nematic volume; the total average energy is essentially constant for each deviation. Thus, if there were no other contributions to the potential energy of the system (such as those arising from buoyancy) and simulations were run in which the shift distance was not fixed but variable then the inclusion could freely move around the volume with essentially no change in energy. This would mean that the resultant probability distribution function would be averaged over all shifts and, since the volume of a spherical shell increases with its radius, the relative contribution to the average distribution would be larger for large shifts; thus we would expect the distribution for a freely moving particle using this particular model would be rather broad ranging from about 40° to 180°. This clearly deviates from the tetrahedral geometry and so we should not expect to obtain a tetrahedral pattern for the defect points on the outer surface. It is useful, therefore, to see if the tetrahedral pattern can be stabilised for non-centrosymmetric shells.

Central tetrahedral inclusions

We start by examining centrosymmetric polyhedral particles, in particular tetrahedrons, since they have the correct symmetry to stabilise four disclinations. It is reasonable to assume that the disclinations in the interior of the shell would locate near the vertices of the polyhedral particle, since this would minimise the length of the disclination lines between the inclusion and the outer spherical surface.

Central tetrahedral inclusions are modelled using a particle with vertices (t, t, t),

(-*t*, -*t*, *t*), (-*t*, *t*, -*t*) and (*t*, -*t*, -*t*). Snapshots of configurations for $t = 15a$ are shown in Figures 3(a) and (b) and, as for spherical inclusions, two types of configurations are observed in which the director field is either parallel or perpendicular to the shortest path between defects; again, these occur with roughly equal frequency. As shown in Figure 3(c), the probability distribution function calculated at the outer surface is peaked at the tetrahedral angle and we again observe a slight narrowing of the distribution for larger particles. However, it is also clear that the distribution calculated for the inner surface is significantly narrower than for the outer surface. It is clear that the inner surface is pinning the disclinations at the vertices of a tetrahedron and, as shown in Figure 3(a) and (b), that these points are actually the vertices of the tetrahedral inclusion, as we might expect. Thus the director field is planar to the sides of the tetrahedron and the disclinations are essentially pinned at the vertices of the inclusion. Since the angular probability distribution for the inner surface is narrower than that for the outer surface, it must be that the disclinations are not perfectly radial and instead they deviate from this slightly. If the temperature is decreased (or increased), the distribution for the outer surface is observed to narrow (or broaden) whilst that for the internal surface remains essentially unchanged.

Shifted tetrahedral inclusions

We now examine the effect of the position of the tetrahedral inclusion on the arrangement of the disclinations. Due to the anisotropic shape of the particle, the shift from the centre cannot be described by distance alone, as it was for spherical inclusions. Therefore, we shift the tetrahedron along three directions, namely {1, 0, 0}, {1, 1, 0}, {1, 1, 1}, with both positive and negative shifts for the latter. In reality, a shift could be in any direction, but we limit ourselves to these four for simplicity since they cover important orientations, such as when one, two or three vertices approach the outer

surface. Typical snapshots and the angular probability distributions are shown in Figure 4 when the internal tetrahedron is shifted by $d = 15a$; note that at this value, shifting in the {1, 1, 1} direction actually leads to the tetrahedron just breaking the outer spherical boundary although the disorder in this region can still be analysed and the disclination found. Shifting along the {1, 0, 0} direction, as shown in Figures 4(a) and (e), breaks the tetrahedral symmetry observed for the central particle, with its four equivalent vertices, into two pairs of vertices differing in their distance from the outer surface and these pairs give rise to three peaks in the angular probability distribution. Both positive and negative shifts along {1, 1, 1} give rise to three equivalent vertices and a single unique one, leading to two distinct angles. The {1, 1, 0} shift gives rise to one pair and two single unique vertices, which in principle should lead to four different peaks in the angular probability distribution although clearly these overlap significantly. In each case, it is clear that there is deviation from the single peak at the tetrahedral angle. To investigate the influence of the shift distance on this deviation, and to compare to the spherical inclusion, we have fitted multiple Gaussian distributions to the angular probability distribution as before to determine both the location and the width of each peak, taking into account the number of expected peaks and their relative intensities in each case. The total spread of the angular distribution can then be summarised as a function of shift distance, by plotting the peak position plus and minus two standard deviations (the "95% rule"), as shown in Figure 5. It is clear that the more the spherical inclusion deviates from the centre of the droplet, the larger the deviation from the perfect tetrahedral geometry; the three peaks observed diverge in location, broadening the entire distribution. A similar observation is made for the tetrahedral inclusion, although here multiple sets of peaks are observed at different angles due to the different orientations. However, the broadening for the tetrahedral particle is

significantly less than that observed for the spherical inclusion. Not only are the peak widths less broad, the spread of the peak locations is also less for the tetrahedral inclusion. As already noted for the spherical inclusions, we would expect the true distribution for a freely moving tetrahedral inclusion to be averaged over all orientations and deviations from the centre. It appears, therefore, that whilst using a free tetrahedral inclusion would not stabilise a perfect tetrahedral geometry for the defect locations at the outer surface of the droplet, the deviation from the perfect geometry is expect to be significantly less than when a spherical inclusion is used.

Our primary focus in this paper is on tetrahedral inclusions since this shape is clearly most likely to both help induce a four disclination line configuration and stabilise the tetrahedral arrangement of the defects at the exterior surface of the nematic shell. However, it is possible that other polyhedral inclusions may also form interesting defect patterns at the outer surface and to finish we briefly examine the configurations observed for central octahedral and cubic inclusions.

Octahedral inclusions

Octahedral inclusions are modelled using a particle with vertices ($\pm o$,0,0) and similar pairs of coordinates along the y and z axes. Results are shown only for dimensions $o = 26a$, for which the vertices are at the same distance from the centre of the inclusion as for a tetrahedron with $t = 15a$; we note that similar results are observed for other dimensions.

According to the Poincaré-Hopf constraint, we should expect to see a total defect charge of +2 on both the inner and outer surfaces. Since there are six vertices on the inner particle, the disclinations must clearly either deviate from tetrahedral symmetry, at least around the interior particle, or deviate from the vertices, or six disclinations could form but one of these must have a -1/2 charge, where the director

rotates by -180°. As shown in Figure 6, we observe configurations containing four +1/2 disclination lines for octahedral inclusions, and the disclinations again emerge at the vertices of the interior polyhedron. Clearly adding two further disclinations of +1/2 and -1/2 charges adds to the elastic energy and so this is not favoured. Similarly, deviating from the vertices is not favoured either. Concentrating on just the disclinations, two types of configuration are observed, as shown in Figure 6 (a) and (b). One (O1) has four disclinations emerging in a single plane around an equator with two bare vertices similar to poles on opposite sides, whereas the other (O2) has the disclinations emerging from all four vertices of two triangular faces that share a common edge with the two bare vertices at the ends of a single edge, forming a sawhorse type configuration. If the disclinations were to emerge from vertices at random, with the only restriction being a maximum of one disclination from each vertex, then we would expect to observe ${}^{6}C_{4} = 15$ different configurations, three of these being of type O1 and the other twelve of type O2; thus we would expect to observe the O2 configuration four times more often than O1 if the energies of these two configurations were equal. The relative occurrence can easily be monitored through the angular distribution function. This is because the relative intensities of the 90˚ and 180˚ peaks will have the ratios 4:2 and 5:1 for the O1 and O2 configurations, respectively. Thus the areas of the peaks should occur in the ratio 72:18 (or 4:1) if the disclination locations are completely random. However, the observed ratio is 2.65:1, indicating that O1 occurs more frequently than it should compared to the random case. This peak ratio corresponds to a ratio of approximately 7:4 for the observation of configuration type O1 compared to O2. Thus O1 must clearly be more stable than O2 for it to occur more frequently than the expected 1:4 for the random case. This can indeed be confirmed in that the energy of the configuration is lower. This is also supported by the observation that if the system is rapidly quenched

into the nematic from the isotropic phase (so no slow cooling equilibration period), then O2 is observed significantly more frequently since the defects are essentially pinned to the vertices once they form and thermal energy is not enough to overcome the barrier of the disclination sliding from one vertex to a neighbouring one.

Cubic inclusions

Cubic inclusions are modelled using a particle with vertices ($\pm c$, $\pm c$, $\pm c$). As before, results are shown only for dimensions $c = 15a$ and we again note that similar results are observed for other dimensions.

As for the other polyhedra, configurations containing four +1/2 disclination lines emerging from vertices of the interior polyhedron are again observed for cubic inclusions, as shown in Figure 7. Based on the symmetry of the cube, it is possible for the disclinations to form a tetrahedral geometry if they emerge from four vertices that are all on mutual face diagonals and we can speculate that this would be the lowest energy state since the disclinations emerge from the central cube from vertices in which the distances between all pairs are maximised. However, four different defect configurations (C1-4) were observed in total on slow cooling, as shown in Figure 7, although in principle another two (C5 and C6) could exist. If we again assume that the disclinations were to emerge from vertices at random, then we would expect to observe ${}^{8}C_{4} = 70$ different configurations and these break down into: C1, 6 configurations; C2, 2; C3, 24; C4, 24; C5, 8; C6, 6. Thus, if the configurations were all of equal energy and had equal probability of occurring then we would expect to see these in the ratio 8.57% : 2.86% : 34.29% : 34.29 % : 11.43 % : 8.57%. The observed probabilities (determined from the angular probability distribution) are 37.3% : 32.4% : 18.8% : 11.5% : 0% : 0%, indicating that C1 and C2 occur more frequently than random whereas the others occur less frequently (if at all). The measured energies of the

configurations follow the trend C2<C1<C3<C4, which is easily understood considering the distance between the locations at which the defects emerge. It is understandable why C5 and C6 are not observed for central cubic particles, given the very close proximities of the disclinations in these configurations. Thus the main point of interest here is why C1 is observed more than C2 despite being higher in energy and this is clearly down to the higher degeneracy of C1 compared to C2. We note here that if the simulations are rapidly quenched from the isotropic phase deep into the nematic region, then the probabilities of the different configurations occurring are much closer to the expected values for random locations although a number of configurations with either one or two escaped defects are also observed. Thus it appears that once the disclinations or 3D escaped defects form at low temperature, the barrier to them either converting from escaped defects to disclinations or for disclinations to slide along a cube edge is relatively high and this process is essentially forbidden. It may be that slowing the cooling rate during the equilibration period, or using an annealing process remaining below the nematic to isotropic transition temperature, could lead to the systematic generation of lowest energy state, thus the tetrahedral pattern for cubes; similarly it may be possible to produce only the four defects in a ring structure for octahedral particles.

Preliminary simulations for non-centrosymmetric octahedrons and cubes were also run, although not in large enough quantity to provide statistically relevant probability distribution functions. However, the results are as we might expect based on the frustration between minimising the total length of the disclination lines and the increased elastic energy forcing the disclinations towards the same volume of space. For example, if the cubic inclusion is moved along an axis then the configuration with disclinations emerging from the vertices on a single side (C6) can be observed, albeit still relatively rarely.

Conclusions

Nematic shells have attracted considerable attention in recent years due to the interesting aspects of frustration in ordering arising from the confinement, the alignment at the surfaces and the total curvature in these systems. One of the key driving requirements for these systems to be useful as 'decorated' colloidal particles is the ability to routinely direct the locations of the defects at the outer spherical surface in a consistent way. A major problem with sphere in sphere shells is that the defects do not form in a tetrahedral pattern if the shells are not concentric. Our simulation results have shown that using solid tetrahedral inclusions, rather than the necessarily spherical liquid ones that have been studied extensively, can lead to a significantly narrower angular distribution function for centralised particles and thus leads to defects on the outer surface that are closer, on average, to being in a tetrahedral arrangement. If the constraint that the particle is fixed at the centre, which is unrealistic for nematic shells, is lifted then the angular distribution is broadened, as it is for spherical inclusions. However, because the disclinations emerge from the interior polyhedral particle vertices, they remain in a configuration that is closer to the tetrahedral pattern than that observed for non-centrosymmetric spheres. Since experimental methods now exist for preparing nematic shells with solid particle interiors, it would be interesting to determine if using polyhedral interiors can help stabilise the tetrahedral defect configuration with respect to both non-tetrahedral defect configurations in non-homogeneous / non-centrosymmetric 'thin' shells and the two escaped +1 defects in 'thick' shells in real systems. The particles studied here have an edge dimension roughly equal to the radius of the droplet and the circumsphere radius is about 2/3 of the outer sphere radius. Larger tetrahedral particles could have been introduced and these would be expected to have a defect arrangement on the outer surface even closer to a

tetrahedron. If it is experimentally possible to introduce similar relatively large particles into nematic shells, then polyhedral particles could be one way of stabilising the tetrahedral defect pattern. Similarly, alternative interior polyhedral particles may prove useful for generating other arrangements of defects at the outer surface.

References

1. Lubensky TC, Prost J. Orientational order and vesicle shape. J Phys II 1992;2:371-382.
2. Nelson DR. Toward a tetravalent chemistry of colloids. Nano Letters 2002;2:1125-1129.
3. Fernandez-Nieves A, Vitelli V, Utada AS, et al. Novel defect structures in nematic liquid crystal shells. Phys Rev Lett. 2007;99:157801.
4. Skacej G, Zannoni C. Controlling surface defect valence in colloids. Phys Rev Lett. 2008;100:197802.
5. Lopez-Leon T, Koning V, Devaiah KBS, et al. Frustrated nematic order in spherical geometries. Nature Physics 2011;7:391-394.
6. Bates MA, Skacej G, Zannoni C. Defects and ordering in nematic coatings on uniaxial and biaxial colloids. Soft Matter 2010;6:655-663.
7. Lopez-Leon T, Bates MA, Fernandez-Nieves A. Defect coalescence in spherical nematic shells. Phys Rev E 2012;86:030702.
8. Bates MA. Nematics on curved surfaces – computer simulations of nematic shells. In: Fernandez Nieves A, Puertas AM, editors. Fluids, colloids and soft materials: an introduction to soft matter physics. Wiley; 2016.
9. Utada AS, Lorenceau E, Link DR, et al. Monodisperse double emulsions generated from a microcapillary device. Science 2005;308:537-541.
10. Sadati M, Zhou Y, Melchert D, et al. Spherical nematic shells with a prolate ellipsoidal core. Soft Matter 2017;13:7465.
11. Kamien RD. The geometry of soft materials: a primer. Rev Mod Phys. 2002;74:953-971.
12. Lebwohl PA, Lasher G. Nematic-liquid-crystal order - a Monte Carlo calculation. Phys Rev A 1972;6:426-429.
13. Fabbri U and Zannoni C. A Monte Carlo investigation of the Lebwohl-Lasher lattice model in the vicinity of its orientational phase transition. Mol Phys. 1986;58:763-788.
14. Chiccoli C, Pasini P, Semeria F, et al. Monte Carlo simulations of model nematic droplets. Mol Cryst Liq Cryst. 1992;212:197-204.
15. Callan-Jones AC, Pelcovits RA, Slavin VA, et al. Simulation and visualization of topological defects in nematic liquid crystals. Phys Rev E 2006;74:061701.
16. Vitelli V, Nelson DR. Nematic textures in spherical shells. Phys Rev E 2006;74:021711.

Figure 1. Snapshots of the disclination lines and director configurations in 'thin' nematic shells with a spherical inclusion ($R = 40a$, $r = 15a$). (a) A concentric shell ($d = 0a$) in which the director field is parallel to the shortest path between a pair of disclinations. (b) A similar shell with the director field perpendicular to this direction. (c) A non-concentric shell ($d = 15a$) in which the disclinations tend to locate in the thinner region near the top of the shell. (d) A 'thick' shell ($R = 40a$, $r = 10a$) in which two escaped +1 defects are observed. In these and all subsequent snapshots, the director field is shown as black streamlines and the disclination lines are shown in blue. Red arrows indicate the distance, d, and direction of any shift of the inclusion.

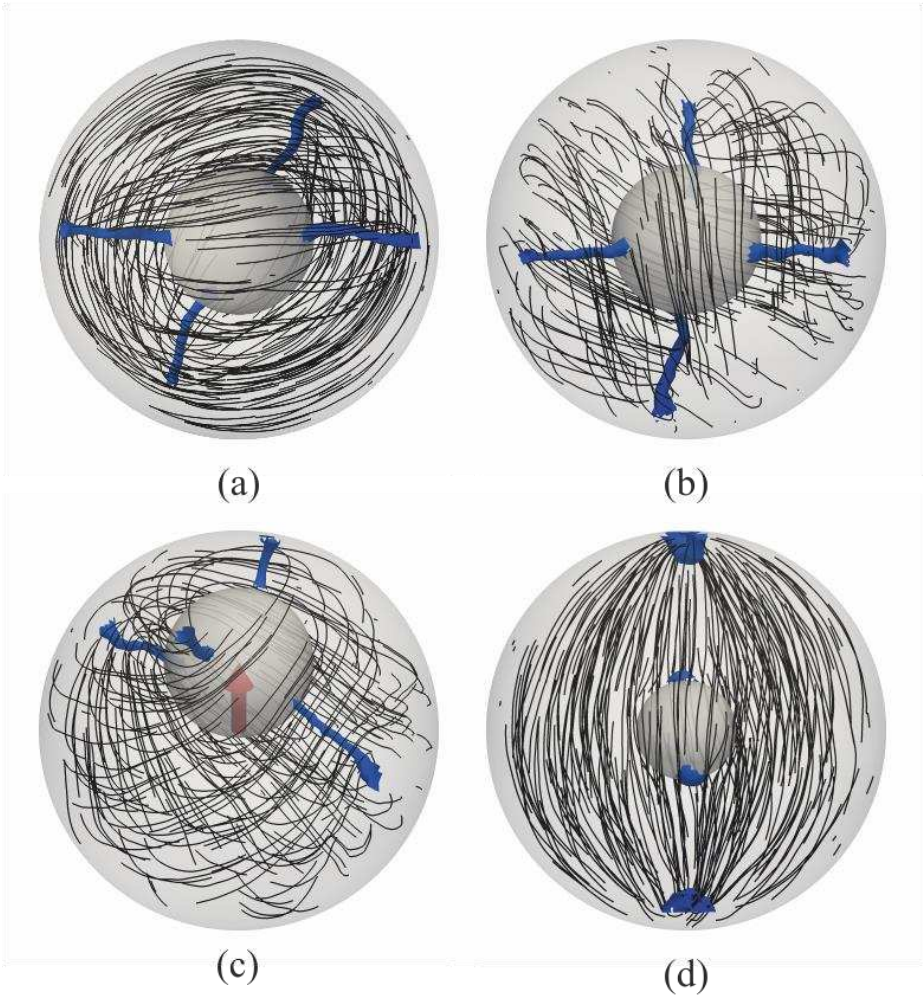

Figure 2. The probability, $f(\theta)$, of finding a pair of disclination lines at a central angle θ for spherical inclusions as a function of the shift for $R = 40a$: (a) $d = 0a$, (b) $5a$, (c) $10a$ and (d) $15a$. The solid points are for smaller inclusions ($r = 15a$) and open points are for larger inclusions ($r = 25a$) with the angle calculated between the centre and the points where the disclinations touch the exterior surface. The grey points in (a) are defined similarly but for the interior surface and for the smaller inclusion only. The lines are best fits using multiple Gaussian distributions (see text).

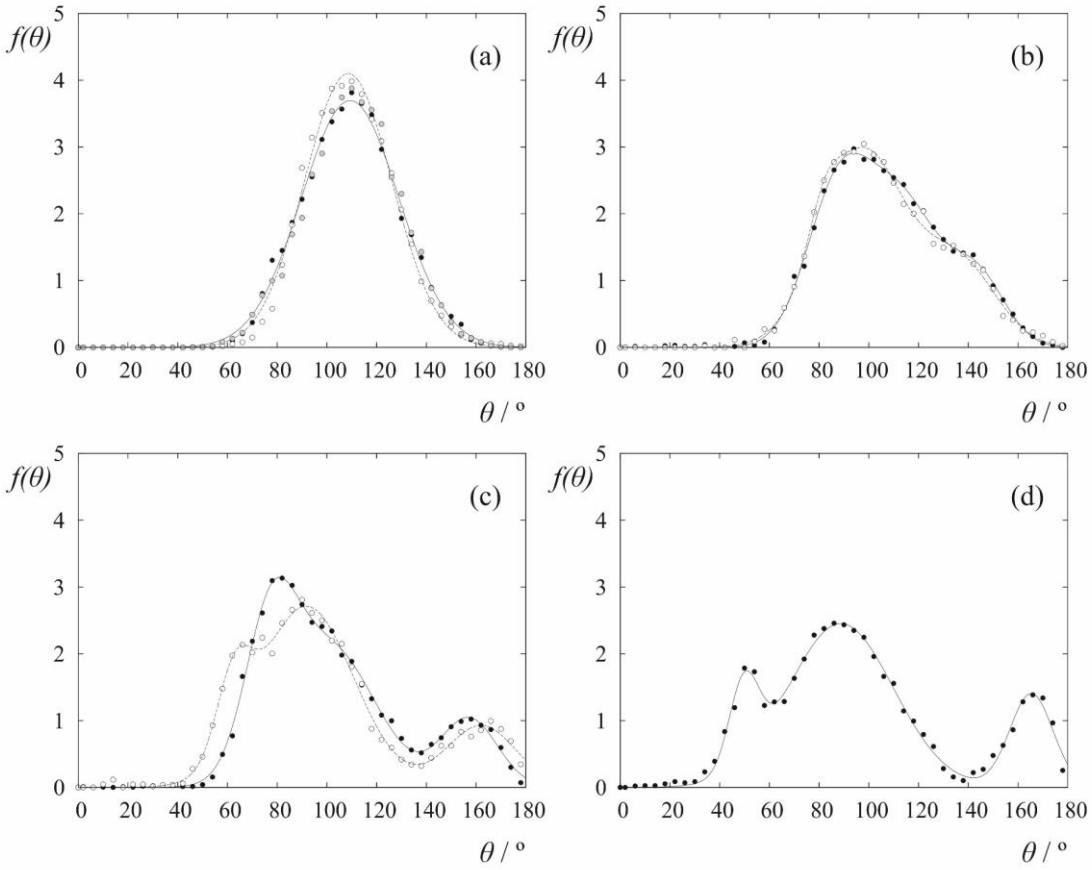

Figure 3. Snapshots of the disclination lines and director configurations in nematic shells with a central tetrahedral inclusion ($R = 40a$, $t = 15a$). In (a) the director field is parallel to the shortest path between the disclination pairs and in (b) it is perpendicular. (c) The angular probability distribution. Solid points are for smaller tetrahedrons ($t = 15a$), open points for larger ($t = 25a$); grey points are the angles at the interior surface for the smaller inclusion only.

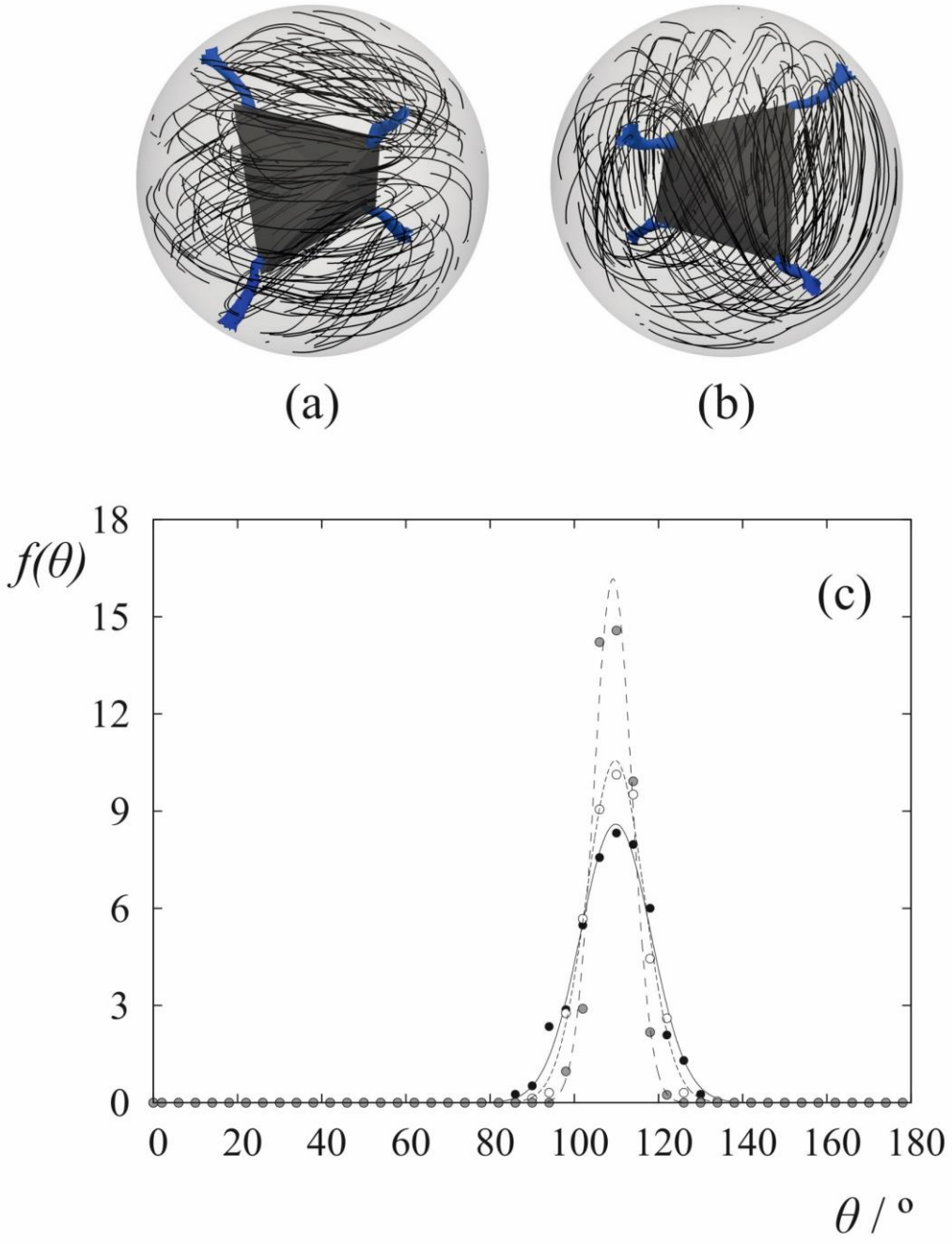

Figure 4. Snapshots of nematic shells ($R = 40a$, $t = 15a$) with shifted tetrahedral inclusions, for a shift of $d = 15a$ along the (a) {1,0,0}, (b) {1,1,0}, (c) {1,1,1} and (d) {-1,-1,-1} directions. (e) - (h) The angular probability distributions (at the exterior surface) for the same shifts.

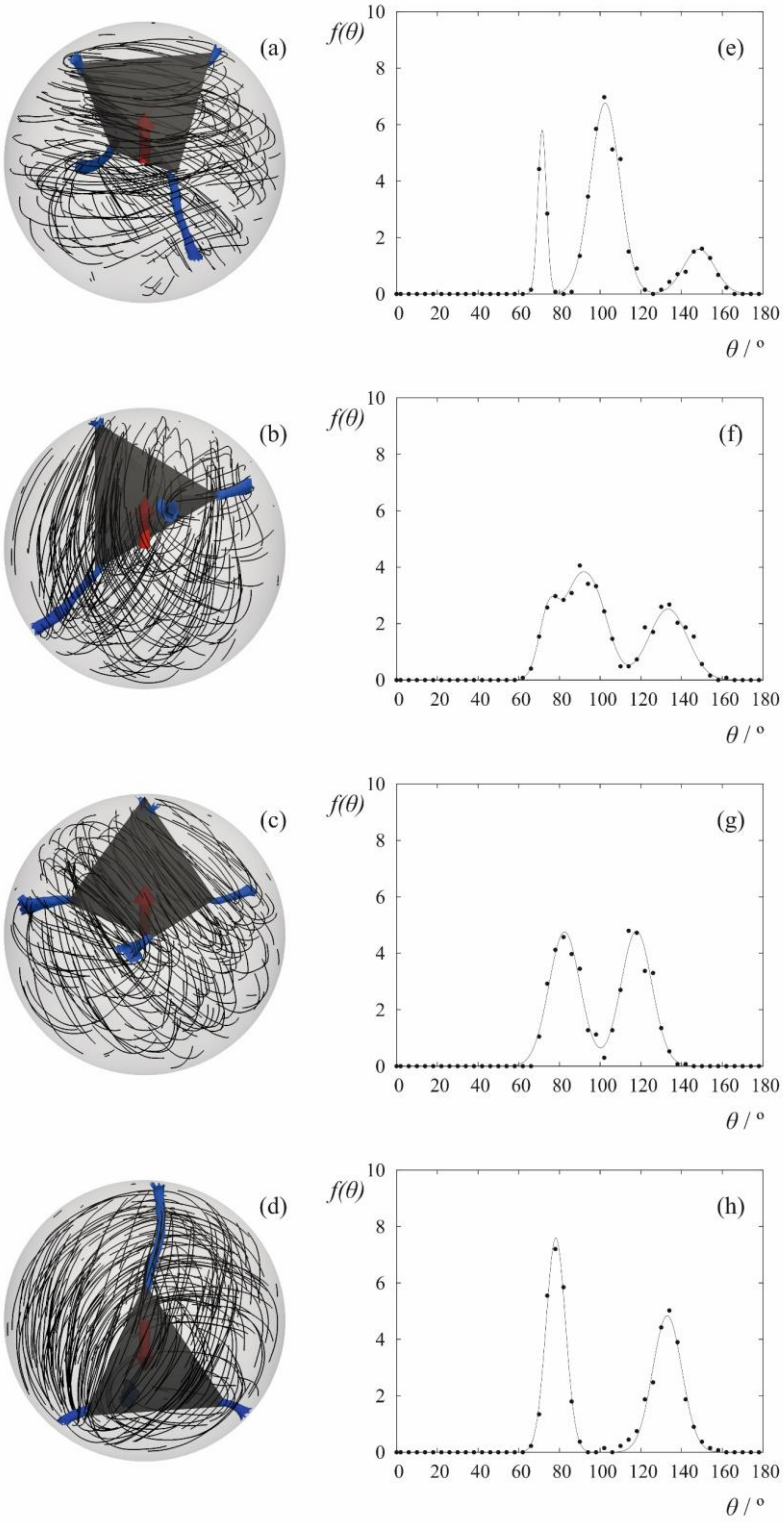

Figure 5. The angular probability distribution at the exterior surface as a function of shift. The peak locations are indicated by solid points for spherical ($r = 15a$) inclusions and open points for tetrahedral ($t = 15a$) inclusions. The multiple points shown for tetrahedrons correspond to shifts along the {1,0,0}, {1,1,0}, {1,1,1} and {-1,-1,-1} directions; the points in the plot are shifted laterally for clarity. The vertical lines have a half-length equal to twice the standard deviation of the Gaussian distributions used to fit the peaks. The dark and light shaded regions represent the approximate spread of the distribution as a function of shift for spherical and tetrahedral inclusions, respectively.

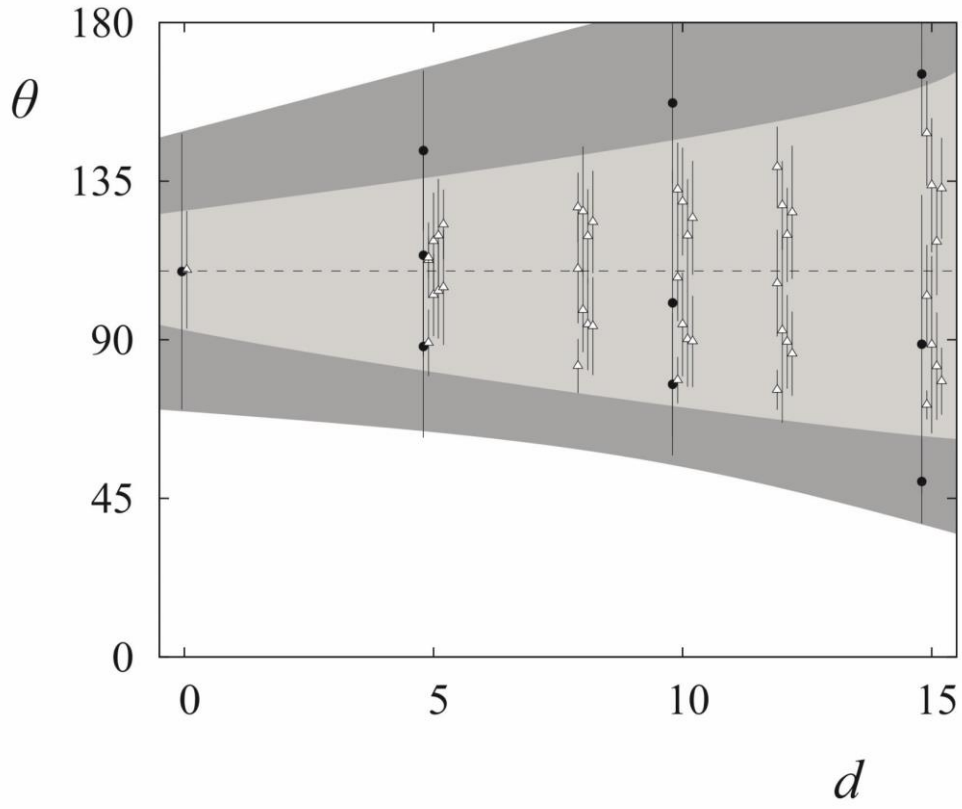

Figure 6. Snapshots and the angular probability distribution for central octahedral inclusions (dimensions $o = 26a$). (a) O1 (63.7%) and (b) O2 (36.3%). Solid points are for the exterior surface, grey points for the interior surface.

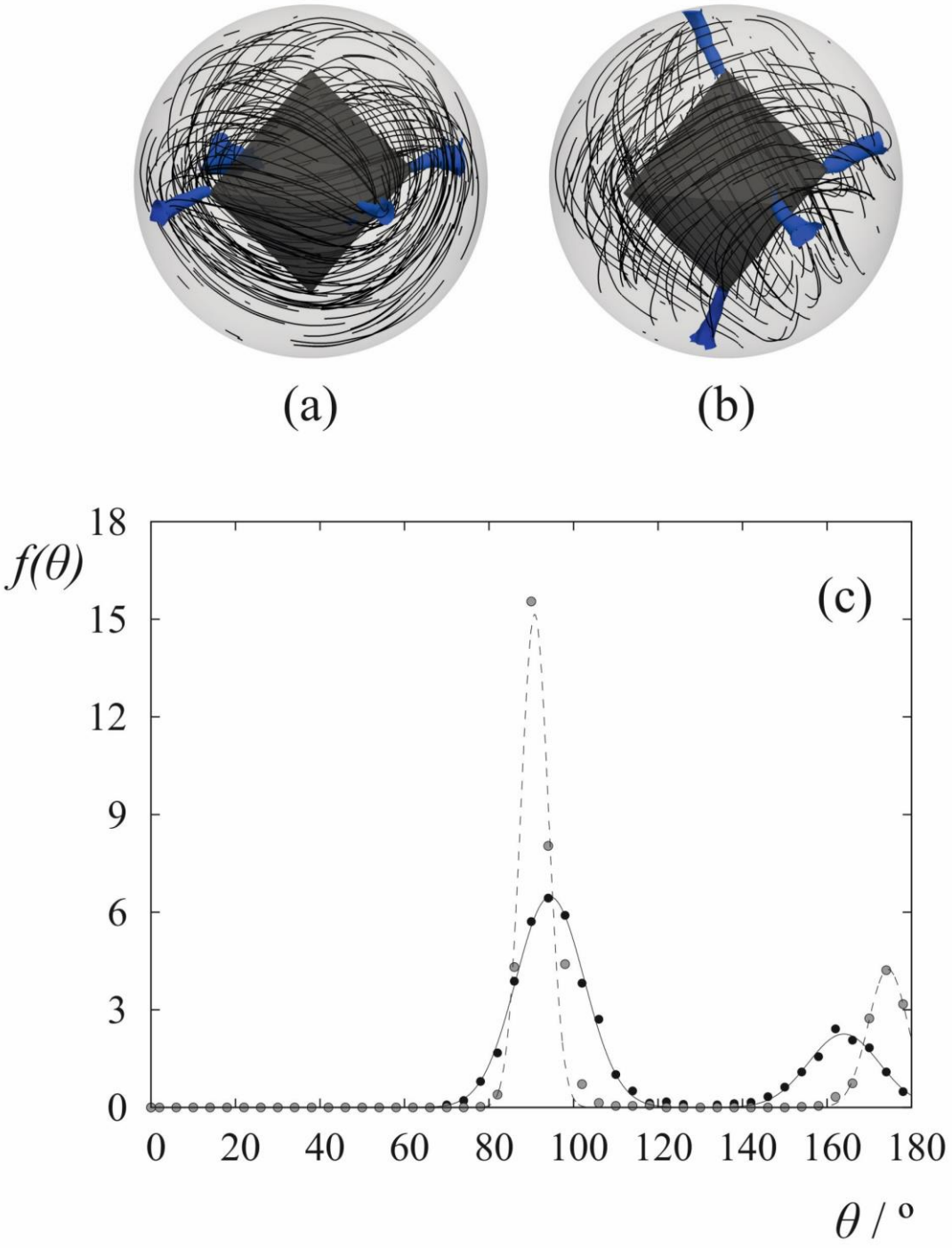

Figure 7. Snapshots and the angular probability distribution for central cubic inclusions (dimensions $c = 15a$). (a) C1 (37.3%), (b) C2 (32.4%), (c) C3 (18.8%), (d) C4 (11.5%), (e) C5 and (f) C6. Solid points are for the exterior surface, grey points for the interior surface.